




# Nanostructured SrTiO<sub>3</sub> with different morphologies achieved by mineral acid-assisted hydrothermal method with enhanced optical, electrochemical, and photocatalytic performances

Shifa Wang<sup>1,2,\*</sup> , Huajing Gao<sup>1,3,\*</sup>, Xianlun Yu<sup>1</sup>, Shengnan Tang<sup>1</sup>, Yong Wang<sup>1</sup>, Leiming Fang<sup>4</sup>, Xinxin Zhao<sup>1</sup>, Jinyu Li<sup>1</sup>, Liang Yang<sup>5</sup>, and Wenqiang Dang<sup>6</sup>

<sup>1</sup> School of Electronic and Information Engineering, Chongqing Three Gorges University, Chongqing, Wanzhou 404000, China

<sup>2</sup> Chongqing Key Laboratory of Geological Environment Monitoring and Disaster Early-warning in Three Gorges Reservoir Area, Chongqing Three Gorges University, Chongqing, Wanzhou 404000, China

<sup>3</sup> School of Science, Lanzhou University of Technology, Lanzhou 730050, China

<sup>4</sup> Institute of Nuclear Physics and Chemistry, China Academy of Engineering Physics, Mianyang 621900, Sichuan, China

<sup>5</sup> Chongqing Institute of Green and Intelligent Technology, Chinese Academy of Sciences, Chongqing 400714, China

<sup>6</sup> School of Electronic Information and Electrical Engineering, Tianshui Normal University, Tianshui 741000, Gansu, China

Received: 22 April 2020

Accepted: 23 August 2020

Published online:

8 September 2020

© Springer Science+Business Media, LLC, part of Springer Nature 2020

## ABSTRACT

SrTiO<sub>3</sub> particles with different morphologies can be produced by hydrothermal reaction route using P25 TiO<sub>2</sub>, Sr(OH)<sub>2</sub>·8H<sub>2</sub>O, NaOH, and mineral acid as the starting materials in the presence of dilute nitric acid solution and heated at 220 °C for 24 h. The dilute nitric acid was replaced by the dilute hydrochloric acid or dilute sulphuric acid, and the reaction time was fine adjusted, and this eventually lead to the formation of nanoparticles or mixing of cubes and nanoparticles. Pure SrTiO<sub>3</sub> can be obtained by changing the mineral acid to nitric acid or hydrochloric acid and adjusting the reaction time from 24 to 40 h. The mineral acid in the synthetic parameter was changed to sulfuric acid, and the synthesized SrTiO<sub>3</sub> sample contained SrSO<sub>4</sub> impurities. The electrochemical investigations confirmed that the performance of SrTiO<sub>3</sub> rhombus particles in terms of rate capability was significantly higher as compared to the SrTiO<sub>3</sub> nanoparticles or mixing of cubes and nanoparticles. Photocatalytic activity test indicated that the SrTiO<sub>3</sub> rhombus particles exhibited an exceptional photocatalytic activity for the removal of congo red dye under simulated sunlight irradiation than that of other SrTiO<sub>3</sub> samples. The variation tendency of photocatalytic activity for different SrTiO<sub>3</sub> samples can be ascribed to the synergistic effects of impurity concentration, energy band, adsorbed oxygen concentration, optical absorption coefficient, charge carrier utilization and separation efficiency, and crystal surface exposure.

Address correspondence to E-mail: wangshifa2006@yeah.net; 20180011@sanxiau.edu.cn; ghj2011@yeah.net

## 1 Introduction

Shape and phase-tunable inorganic metal oxides with different morphologies have drawn much attention on both relevant theories and technologies in recent years because of their fascinating optical, electrochemical properties, and photocatalytic activities and widespread applications in solid-state lighting device, supercapacitor, photocatalyst, and thermoelectric material [1–7]. Generally, the shape and phase-tunable inorganic metal oxides strongly depend on the synthetic method, surface reconstruction and treatment, facet control, band-gap modulation, heterostructure construction, and so on [8–17]. Strontium titanate ( $\text{SrTiO}_3$ ) is an important photocatalyst, it has continually received significant attention due to its low recombination, high charge carrier mobility, and high charge transfer and separation efficiency [18–20]. However, it has two obvious disadvantages for pure  $\text{SrTiO}_3$  which are wide band-gap of 3.2 eV and low visible photocatalytic activity for the photocatalytic degradation of organic dyes [20, 21]. Therefore, a lot of work has been done around overcoming the above-mentioned two shortcomings of pure  $\text{SrTiO}_3$  [22–25]. In the past few years, much works have been devoted to the degradation activity of  $\text{SrTiO}_3$  with different morphologies for the degradation of organic pollutant or photocatalyzed hydrogen production under xenon lamp with emitting simulated sunlight irradiation [26, 27]. Ouyang et al. [28] reported that the nanoporous  $\text{SrTiO}_3$  photocatalysts synthesized by a nano-template-assisted sol-gel hydrothermal reaction method exhibit a high photocatalytic performance for the degradation of organic pollutant under xenon lamp irradiation. Kuang et al. [29] synthesized the single-crystal-like porous  $\text{SrTiO}_3$  nanocubes by a facile hydrothermal reaction method showing an enhanced photocatalytic activity in hydrogen evolution from water splitting under xenon lamp irradiation. Zheng et al. [30] prepared the  $\text{SrTiO}_3$  hollow microspheres by hydrothermal method showing a superior photocatalytic activity in photoreduction of Cr(VI) under xenon lamp irradiation. Li et al. [31] synthesized the cubic-perovskite  $\text{SrTiO}_3$  by a facile solvothermal route displaying a facet-dependent photocatalytic activity for the degradation of rhodamine B and methyl orange under xenon lamp irradiation. Wang et al. [9] reported the surface-reconstructed  $\text{SrTiO}_3$  nanocrystals enclosed with {023} and {001} facets by

introducing oxygen vacancies showing a high photocatalytic activity for the hydrogen evolution under xenon lamp irradiation. Hsieh et al. [10] prepared the shape-tunable  $\text{SrTiO}_3$  crystals by mixing  $\text{TiCl}_4$ ,  $\text{SrCl}_2$ , and  $\text{LiOH}$  in ethanol solution showing that the surface facet control enhances photocatalyzed hydrogen production under xenon lamp irradiation. Up to now, there are only a few reports on the adjust and control for the synthesis of  $\text{SrTiO}_3$  particles with different morphologies by introducing mineral acid and adjusting reaction time for the promoted photocatalytic degradation of organic dyes.

Zhou et al. [32] reported that the  $\text{TiO}_2$  nanoheterostructures with different morphologies synthesized by  $\text{HCl}$  or  $\text{H}_2\text{SO}_4$  with assisted hydrothermal method exhibit enhanced photocatalytic activity and gas-sensitive performance. Zhou and co-workers have developed a facile acid-hydrothermal method to fabricate  $\text{TiO}_2$  microspheres, nanoflowers, nanotrees, and nanobelts by varying the  $\text{HCl}$  concentration and revealed the shape-dependent tuning of photoluminescence properties. [33] Shen et al. [34] synthesized the single-crystalline  $\text{TiO}_2$  nanostructures with different morphologies by a novel inorganic acid ( $\text{HCl}$ ,  $\text{HNO}_3$ , or  $\text{H}_2\text{SO}_4$ )-assisted hydrothermal route showing the morphology, phase purity, composition, crystallite size, and photocatalytic activity of  $\text{TiO}_2$  to have a high dependency in the concentration of inorganic acid. All these studies indicate that introduction of mineral acids to adjust the phase purity and surface morphology could increase oxygen vacancy concentration and enhance optical absorption coefficient and charge transfer ability of semiconductor photocatalyst, resulting in the improved photocatalytic activity for the photocatalytic degradation of organic dyes. Motivated by this,  $\text{SrTiO}_3$  photocatalyst with controllable phase purity and morphology can be prepared by adding mineral acid.

In this paper, we have successfully synthesized different shapes and phase-tunable  $\text{SrTiO}_3$  perovskite-type metal oxides with different morphologies using various mineral acids. Particle shape control from rhombus to nanoparticles to flowers-like and mixing of cubes and nanoparticles were achieved by adopting the strategy of mineral acid and reaction time. The five  $\text{SrTiO}_3$  samples were compared for the phase structure, crystallinity, purity, shape, optical absorption coefficient, oxygen vacancy concentration, charge carrier separation efficiency, and

photocatalytic activity for the photocatalytic degradation of congo red dye under ultraviolet and simulated sunlight irradiation. SrTiO<sub>3</sub> rhombus particles have been found to exhibit the best optical absorption coefficient, charge transfer and separation efficiency, and photocatalytic activity, demonstrating that shape control is a fascinating direction for improving physicochemical properties of metal oxide semiconductor materials. Based on these results, a possible photocatalytic mechanism involved in the photo-degradation of congo red dye using pure SrTiO<sub>3</sub>, O (oxygen vacancy)—SrTiO<sub>3</sub>, or I (impurity)—SrTiO<sub>3</sub> was proposed.

## 2 Experimental procedure

### 2.1 Synthesis of SrTiO<sub>3</sub> with different morphologies

Stoichiometric amounts of commercial P25 TiO<sub>2</sub> and Sr(OH)<sub>2</sub>·8H<sub>2</sub>O powders (99%) were mixed in 60 mL deionized water to obtain mixed solution with molar ratio of Sr:Ti = 1: 1. After that 3 mL mineral acid (HNO<sub>3</sub>, HCl, or H<sub>2</sub>SO<sub>4</sub> with analytically pure grade) and 9.9993 g sodium hydroxide with analytically pure grade were added to the above solution. All the above processes are carried out under the action of magnetic stirring. After two hours, the solution was transferred to a high-pressure reactor with polytetrafluoroethylene lining, and the precursor products were obtained at 220 °C for different reaction times (24 and 40 h). The excess alkali was removed by cooling and cleaning with deionized water and ethyl alcohol to obtain the solid product. Finally, the solid product was dried at 60 °C for 5 h to obtain the final product. The samples prepared at 3 mL HNO<sub>3</sub> and HCl and reaction time at 24 h were denoted as S1 and S3, respectively. Whereas the samples prepared at 3 mL HNO<sub>3</sub>, HCl, and H<sub>2</sub>SO<sub>4</sub> and reaction time at 40 h were denoted as S2, S4, and S5, respectively. Figure 1 shows the chemical route for the preparation of SrTiO<sub>3</sub>.

### 2.2 Material characterization

The phase structure, purity, and component of Samples S1, S2, S3, S4, and S5 were analyzed by a D8 advanced type X-ray diffractometer with CuK $\alpha$

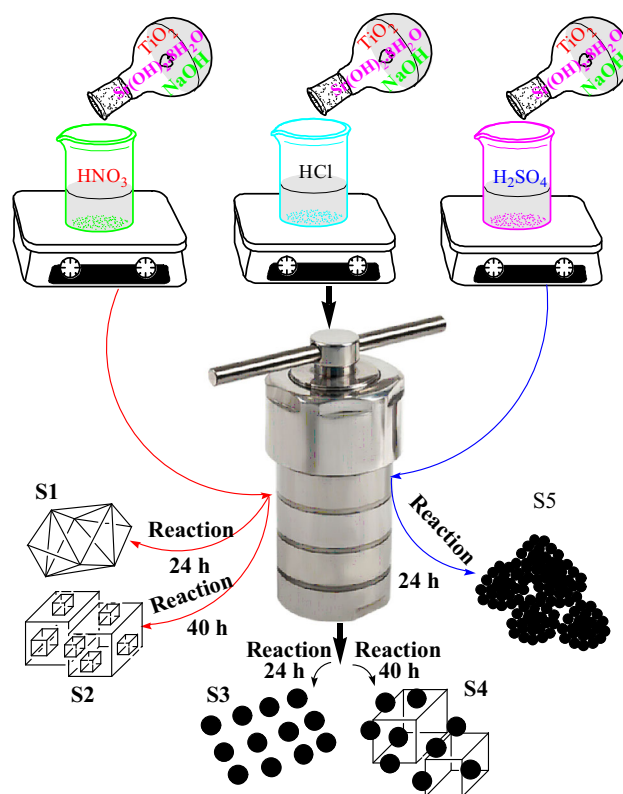


**Fig. 1** Chemical route for the preparation of SrTiO<sub>3</sub>

radiation at a wavelength of 0.15406 nm and operated at 40 kV and 30 mA. The surface morphology of Samples S1, S2, S3, S4, and S5 were characterized by a JSM-6701F-type field-emission scanning electron microscopy (FE-SEM). Ultraviolet–Visible (UV–Vis) diffuse reflectance spectra of Samples S1, S2, S3, S4, and S5 were measured on a UV–Vis spectrophotometer and BaSO<sub>4</sub> used as the reference. X-ray photoelectron spectroscopy (XPS) was used to measure the charge state, chemical component of Samples S1, S2, S3, S4, and S5 by a KRATOS X SAM 800 X-ray photoelectron spectrometer. The electrochemical properties of Samples S1, S2, S3, S4, and S5 were investigated on a CHI760E electrochemical workstation using a three-electrode cell configuration. The experiment was similar to the literature [11] except changing the working electrode and electrolyte as SrTiO<sub>3</sub> and 1 mol L<sup>-1</sup> KOH aqueous solution, respectively. The slurry was evenly dispersed on the nickel foam with area of 1 cm × 1 cm and transferred to the thermostat drying oven to dry at 60 °C for 5 h. The photocatalytic degradation experiments of Samples S1, S2, S3, S4, and S5 were described in literature [11]. 100 W/m<sup>2</sup> high-pressure mercury

lamp and 150 W xenon lamp are used to emit UV-light and simulated sunlight ( $290 < \lambda < 800$  nm), respectively. According to literature [35], the hole ( $h^+$ ), hydroxyl radical ( $\cdot OH$ ), and superoxide radical ( $\cdot O_2^-$ ) can be detected by disodium ethylenediaminetetraacetic acid (EDTA-2Na), 2-propanol (IPA), and 1,4-benzoquinone (BQ), respectively. The EDTA-2Na, IPA, and BQ are used as scavengers. The trapping experiment was similar to above photo-degradation experiment of congo red dye except the addition of 1 mmol scavengers in the photocatalytic reaction system.

### 3 Results and discussion

#### 3.1 Structural analysis

The phase structure, purity, and composition of all  $SrTiO_3$  samples have been identified on the basis of the respective XRD patterns as shown in Fig. 2. The XRD results were fitted by MDI Jade 6.0 package. The black curve, red curve, vertical line, and blue line represents the experiment value, calculated value, Bragg peak, and the difference between the experiment and calculated values, respectively. The results indicate that the calculated results are in good match with the observed XRD diffraction peaks. All XRD diffraction peaks can be assigned to (100), (110), (111), (200), (210), (211), (220), (300), (310), (311), and (222). For the Samples S1, S2, S3, and S4, they are all pure cubic  $SrTiO_3$  perovskite-type oxides with standard JCPDF card no. 35–0734. There was no significant difference in diffraction peak position among the four samples, despite changes in the mineral acid, and reaction time [Fig. 2a, b, c, and d]. In Fig. 2e, Sample S5 presents the mixed phases of  $SrTiO_3$  with standard JCPDF card no. 35-0734 and  $SrSO_4$  with standard JCPDF card no. 05-0593. As to strong sulfuric acid ( $H_2SO_4$ ), it was stopped being used to synthesize the  $SrTiO_3$  fine particles as  $H_2SO_4$  can react easily with strontium (Sr) ion and form  $SrSO_4$  precipitates. The mean crystallite sizes ( $D$ ) of Samples S1, S2, S3, S4, and S5 were calculated on the basis of line broadening of (110), (111), and (200) peaks using the Scherrer's Eq. (1) are about to be 135.7046, 93.1833, 83.2245, 100.5236, and 38.6325 nm, respectively.

$$D = \frac{k\lambda}{\beta \cos \theta}, \quad (1)$$

where  $k$  is the shape factor, the value is generally between 0.62 and 2.08 on the basis of different morphologies [36–38],  $\beta$  is the full-width at half maximum (FWHM) of x-ray peak,  $\lambda$  is the X-ray wavelength, and  $\theta$  is the Bragg diffraction angle.

The cell parameter ( $a$ ) and unit cell volume ( $V$ ) of Samples S1, S2, S3, S4, and S5 were also calculated by Eqs. (2) and (3).

$$\frac{1}{d^2} = \frac{(h^2 + k^2 + l^2)}{a^2}, \quad (2)$$

where  $d$  and ( $h, k, l$ ) are the interplanar spacing and plane indices of  $SrTiO_3$  crystal, respectively.

$$V = a^3 \quad (3)$$

The calculated mean crystallite size, cell parameter, and unit cell volume for different samples are shown in Table 1. As can be seen from Table 1, Sample S3 has the smallest mean crystallite size, largest cell parameter, and unit cell volume than that of other samples. As for  $HNO_3$ , the crystallite size decreased with the increasing of reaction time, while HCl showed the opposite trend. Figure 2f shows the crystal structure of  $SrTiO_3$ . The cubic  $SrTiO_3$  perovskite-type oxides possess a Pm3m symmetry. For the  $ABO_3$  structure, the oxygen (O) and titanium (Ti) atoms form a perfect octahedron due to the O atom located in the face-center positions of cubic unit cell, while the strontium (Sr) atom lying outside the oxygen octahedron [39].

#### 3.2 Morphology analysis

The morphologies of  $SrTiO_3$  perovskite-type oxides with different acids and reaction times are displayed in Fig. 3. Figure 3a shows the typical SEM images of  $SrTiO_3$  rhombus particles with  $HNO_3$  and reaction 24 h. The rhombus particles are non-uniform, with smooth and clean surfaces. The particle size ranges up to several tens to several hundreds of nanometer. Figure 3b illustrates the SEM image of cubic-like  $SrTiO_3$  aggregates with different size ranges treated by  $HNO_3$  and reaction 40 h. The hydrothermal synthesis conditions inhibited grain irregular growth remarkably, and the particle size of cubic-like  $SrTiO_3$  aggregates clearly became polarized. The  $SrTiO_3$

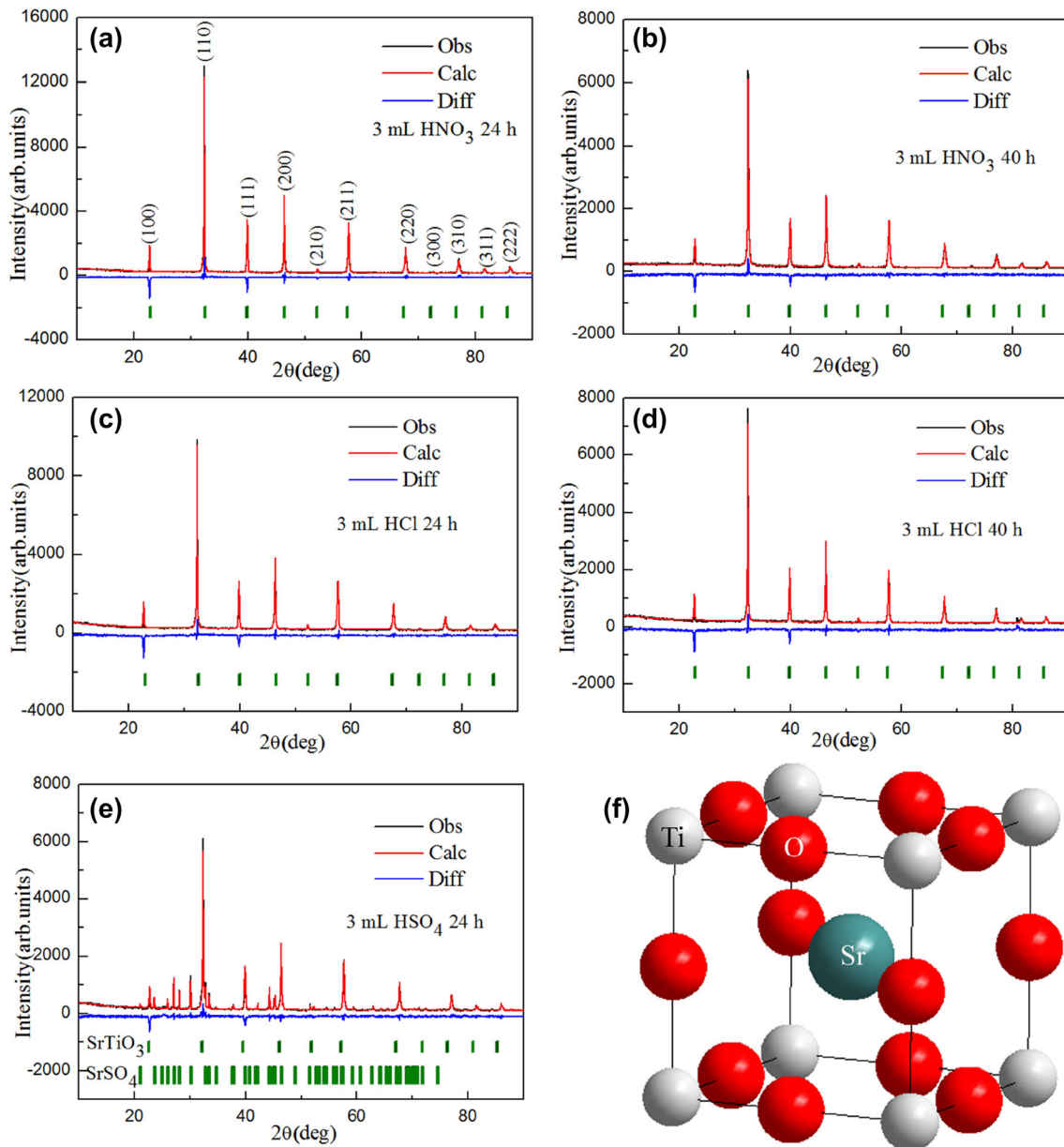


**Fig. 2** XRD patterns and crystal structure of SrTiO<sub>3</sub>. **a** S1, **b** S2, **c** S3, **d** S4, **e** S5, and **f** crystal structure

**Table 1** Unit cell volume, crystallite size, interplanar spacing value, and cell parameter of Samples S1, S2, S3, S4, and S5

Sample	Unit cell volume (Å <sup>3</sup> )	Crystallite size (nm)	d of SrTiO <sub>3</sub> diffraction peaks /(Å)			Cell parameter a(Å)
			(110)	(111)	(200)	
S1	59.8132	135.7046	2.7650	2.2570	1.9553	3.9108
S2	59.9004	93.1833	2.7600	2.2538	1.9522	3.9127
S3	59.9785	83.2245	2.7667	2.2591	1.9568	3.9144
S4	59.8774	100.5236	2.7651	2.2571	1.9554	3.9122
S5	59.8958	38.6325	2.7651	2.2580	1.9554	3.9126

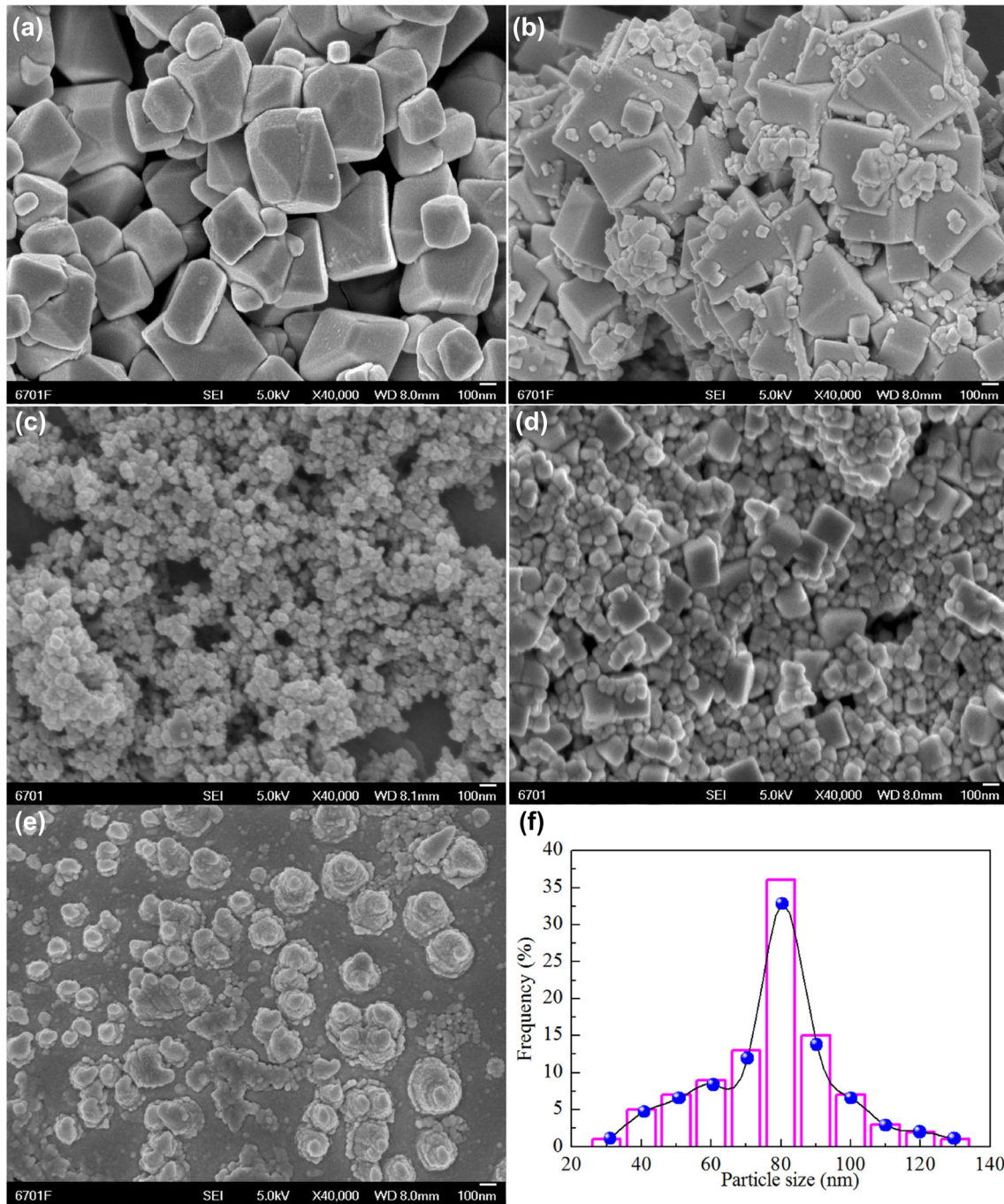


**Fig. 3** SEM images and particle size distribution of SrTiO<sub>3</sub>. **a** S1, **b** S2, **c** S3, **d** S4, **e** S5, and **f** particle size distribution for the Sample S3

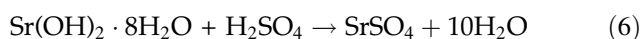
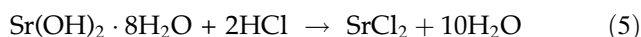
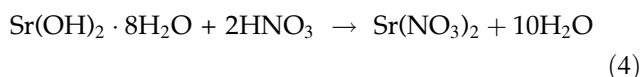
nanoparticles were synthesized by the HCl-assisted hydrothermal process at 220 °C for 24 h, without using other organic additives, which is shown in Fig. 3c. The mean particle size of SrTiO<sub>3</sub> nanoparticles is around 80 nm as shown in Fig. 3f. As the reaction time increased to 40 h, the cubic-shaped SrTiO<sub>3</sub> particles appeared in the sample as shown in Fig. 3d. It is worth noting that increasing the reaction

time of either hydrochloric acid or nitric acid in assisted hydrothermal synthesis process can cause the SrTiO<sub>3</sub> particles to be large and small. The particle size of SrTiO<sub>3</sub> particles observed by SEM images is larger than that of crystallite size calculated by XRD results as the particle may contain a few crystals [40]. Figure 3f shows the SEM image of SrTiO<sub>3</sub> particles with H<sub>2</sub>SO<sub>4</sub> and reaction at 24 h. In Fig. 3f, the

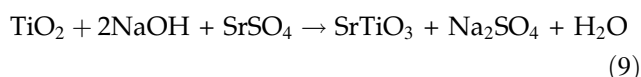
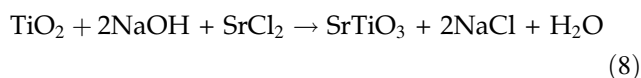
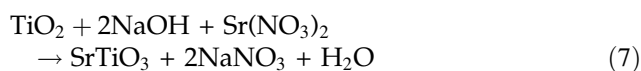
flowerlike nanostructures with an average particle size of 40 nm were confirmed. Acid type and reaction time are crucial for the formation of SrTiO<sub>3</sub> particles with different morphologies.

### 3.3 Plausible formation mechanism of SrTiO<sub>3</sub> particles with different morphologies

When the inorganic acid is absent from the precursor solution, Sr(OH)<sub>2</sub>·8H<sub>2</sub>O is easy to react with the metastable phase of anatase TiO<sub>2</sub> in the P25 TiO<sub>2</sub> to produce cubic shape of SrTiO<sub>3</sub> particles [41–43]. When the inorganic acid is introduced into the precursor solution, Sr(OH)<sub>2</sub>·8H<sub>2</sub>O can react with the inorganic acid first, and its chemical reaction equations are shown as follows.



Subsequently, the titanium dioxide can react with the sodium hydroxide and strontium salt to form strontium titanate. The relevant chemical equations can be described in detail as follows:



SrSO<sub>4</sub> is very stable, so it is very difficult to react with TiO<sub>2</sub> and NaOH. Therefore, the presence of SrSO<sub>4</sub> was observed in sample S5 as shown in Fig. 2e. It is worth noting that the inorganic acid was added very little throughout the experiment. This is just one part of reaction process. Other reaction processes can be described in literature [43]. Several reaction processes in the precursors lead to the unevenness of the resulting strontium titanate particles. According to the literatures [44, 45], the TiO<sub>2</sub> consists of TiO<sub>6</sub><sup>2-</sup> octahedra with different coordination modes to form the metastable anatase and stable rutile phases. Under the action of OH groups, TiO<sub>6</sub><sup>2-</sup> octahedron in the TiO<sub>2</sub> is easy to bridge with it. Several TiO<sub>6</sub><sup>2-</sup>

octahedrons coordinate with Sr ions in strontium nitrate to form strontium titanate with a rhombus structure as shown in Fig. 3a. For the strontium chloride, only the vertex positions of two TiO<sub>6</sub><sup>2-</sup> octahedrons are bridged with strontium ions, resulting in the formation of SrTiO<sub>3</sub> spherical particles as shown in Fig. 3c. As the reaction time increased, the strontium titanate particles gradually regained their cubic shape due to the steric repulsion and thermodynamically stable [45]. It can be seen that the morphology of SrTiO<sub>3</sub> highly depends on the structure of strontium salt formed during the intermediate process and reaction time.

### 3.4 Optical properties

Figure 4a shows the UV–Visible diffuse reflection spectra of Samples S1, S2, S3, S4, and S5. In the wavelength range of 200–320 nm, the reflectance for each sample is almost constant. In the wavelength range of 320–400 nm, the reflectance for each sample is dramatically increase. Above 400 nm, the reflectance increased slowly with increasing of wavelength. Under careful identification of UV–Visible diffuse reflection spectra in Fig. 4a, the lower reflectance of Sample S5 in the ultraviolet region was found toward shorter wavelengths, indicating that the reflectance behavior might be affected by the SrSO<sub>4</sub> impurity. The relative parameters including color parameters (CIE L\*, a\*, b\*), hue angle (H°), chroma (c\*), and total color difference (ΔE<sub>CIE</sub><sup>\*</sup>) of Samples S1, S2, S3, S4, and S5 can be estimated by literatures [46–49] and are shown in Table 2. The result of white color is mainly governed by the color parameter L\*: the larger L\* value represents the more intense white color of SrTiO<sub>3</sub> perovskite-type oxides. At the same time, the largest L\* value also represents the lightness of SrTiO<sub>3</sub> perovskite-type oxides. As can be seen from Table 2, Sample S5 has a largest L\* value implying that Sample S5 has the brightest white color. The real photos of Samples S1, S2, S3, S4, and S5 are shown in Fig. 4d. The color of SrTiO<sub>3</sub> samples is consistent with the results in Table 2.

The UV–Vis absorption spectra of Samples S1, S2, S3, S4, and S5 were calculated using the Kubelka–Munk (K–M) equation and UV–vis diffuse reflectance spectra. Figure 4b shows the UV–Vis absorption spectra of Samples S1, S2, S3, S4, and S5. Two obvious absorption bands at 200–400 (Fig. 4b) and 400–800 nm (enlargement inset in Fig. 4b) can be

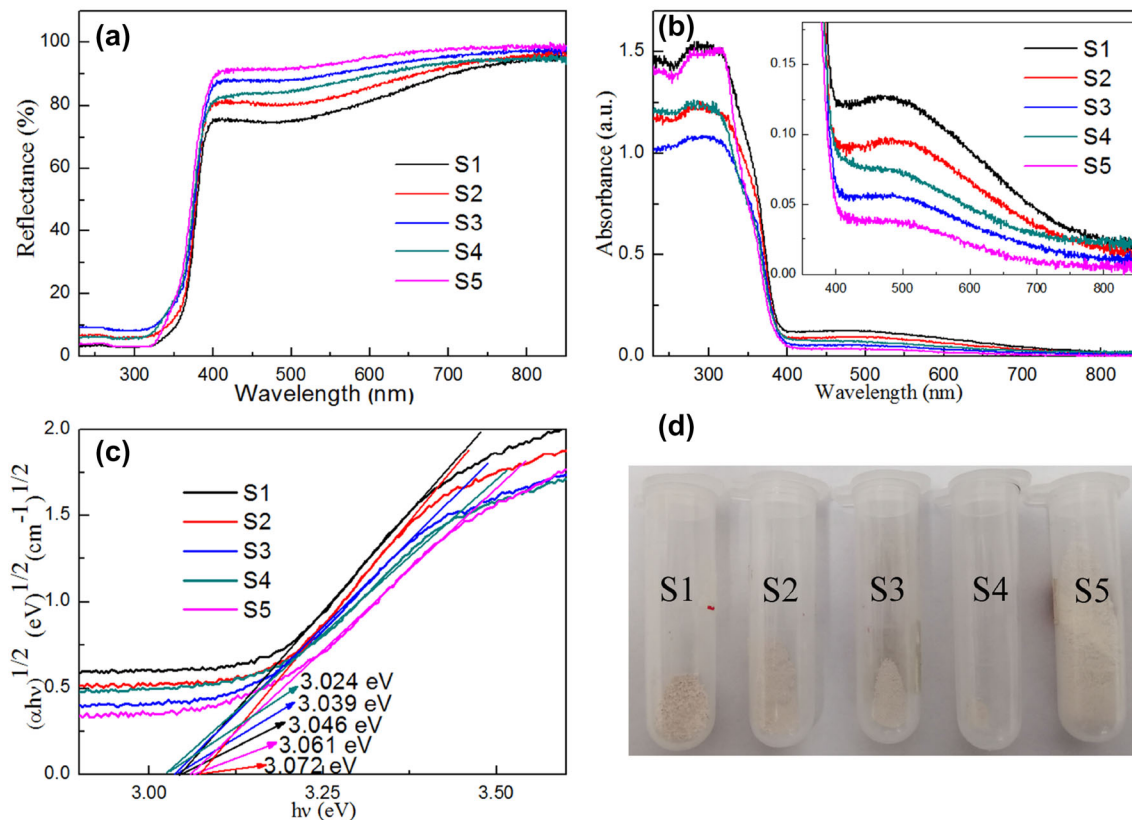


**Fig. 4** a UV–Visible diffuse reflection spectra, b UV–Vis absorption spectra, c optical band-gap ( $E_g$ ) values, and d real photos of Samples S1, S2, S3, S4, and S5

**Table 2** Color coordinates and  $E_g$  values of Samples S1, S2, S3, S4, and S5

Sample	Color coordinates						$E_g$ value (eV)
	L*	a*	b*	c*	H°	$\Delta E_{CIE}^*$	
S1	90.947	2.851	2.582	3.846	42.165	91.028	3.046
S2	93.018	2.518	1.746	3.064	34.738	93.068	3.072
S3	96.034	1.478	1.569	2.156	46.711	96.058	3.039
S4	94.772	1.599	2.408	2.891	56.414	94.816	3.024
S5	97.407	1.150	1.432	1.837	51.233	97.424	3.061

observed. Two absorption bands are assigned to the intrinsic band-gap adsorption [29, 43, 50] and oxygen vacancy [9] of SrTiO<sub>3</sub>, respectively. The existence of oxygen vacancy can be further confirmed by XPS spectra. In Fig. 4b, Sample S1 exhibits the strongest ultraviolet and visible absorption coefficient, while Sample S5 shows a lowest visible absorption coefficient due to the effect of SrSO<sub>4</sub> impurity. It can be seen that the ultraviolet and visible absorption coefficient of SrTiO<sub>3</sub> samples follows the order: S1 > S5 > S4 > S2 > S3 and S1 > S2 > S4 > S3 > S5, respectively.

The optical band-gap ( $E_g$ ) values of Samples S1, S2, S3, S4, and S5 can be obtained from  $\alpha$  as a function of wavelength from the Tauc relation [41–56]. The  $E_g$  values of Samples S1, S2, S3, S4, and S5 can be obtained from the intercept of the straight line portion of  $(\alpha hv)^{1/2}$  versus  $h\nu$  plot to  $(\alpha hv)^{1/2} = 0$ . Figure 4c shows the  $E_g$  values of Samples S1, S2, S3, S4, and S5. The  $E_g$  values of Samples S1, S2, S3, S4, and S5 are found to be 3.046, 3.072, 3.039, 3.024, and 3.061 eV, respectively. The variation tendency is inconsistent with the results of SEM observation, XRD calculation, and previous reports [57] due to the effect of different morphologies.



### 3.5 XPS analysis

To confirm the chemical composition and oxygen vacancy of Samples S1, S2, S3, S4, and S5, XPS spectra of Samples S1, S2, S3, S4, and S5 are measured by a x-ray photoelectron spectrometer. The survey scan XPS spectra of Samples S1, S2, S3, S4, and S5 are shown in Fig. 5a. It can be confirmed that the major elemental compositions of Samples S1, S2, S3, S4, and S5 are Sr, Ti, O, and C. The C 1s characteristic peak at 284.2 eV can be ascribed to the calibration peak of XPS instruments [58].

Figure 5b–f shows the O1s high-resolution XPS spectra of Samples S1, S2, S3, S4, and S5. For Samples S1, S2, S3, and S4, the O1s peak in the wide range can be resolved into two peaks at 528.71–528.92 and 530.11–530.19 eV ascribed to lattice oxygen ( $O_L$ ) [59] and adsorbed oxygen ( $O_A$ ) [60, 61], respectively. The deconvoluted O 1s characteristic peaks of Sample S5 mainly comprised oxygen in lattice oxygen about at 528.83 eV, adsorbed oxygen at 529.92 eV, and the oxygen in the sulfate group (S-O) at 531.76 eV [62] as shown in Fig. 5f. The  $O_A/O_L$  molar ratios of Samples S1, S2, S3, S4, and S5 are summarized in Table 3. The result shows that Sample S5 has a minimum value, which exhibits a worst photocatalytic activity. The remaining samples can only identify the existence of oxygen vacancies in the samples, but it is difficult to distinguish the concentration of oxygen vacancies.

### 3.6 Electrochemical properties

#### 3.6.1 Electrochemical impedance spectroscopy (EIS) analysis

EIS technology was applied to understand the charge transfer process of SrTiO<sub>3</sub> samples. Figure 6 shows the EIS spectra of Samples S1, S2, S3, S4, and S5. Only a straight line can be observed for the Samples S1, S2, S3, S4, and S5 as the semicircle is barely visible. The straight line can be assigned to the Warburg impedance [63]. The angle between the straight line and X-axis for the Samples S1, S2, S3, S4, and S5 follows the order: S1 > S5 > S2 > S3 > S4. This large angle usually means that the radius of the semicircle is smaller. The smallest arc radius on EIS spectra of SrTiO<sub>3</sub> sample means a fast interfacial charge transfer and high charge separation efficiency [64–68]. The results imply that the Sample S1 have a highest

photocatalytic activity for the photocatalytic degradation of organic dyes.

#### 3.6.2 Cyclic voltammetry (CV) studies

Cyclic voltammetry (CV) is an excellent method to analyze electrochemical properties of electrodes. Figure 6a–e shows the CV curves of Samples S1, S2, S3, S4, and S5 measured at the scan rates of 3, 5, 10, 20, 30, 40, 50, and 100 mV·s<sup>-1</sup> in the potential range of 0–0.5 V. For the Samples S1, S2, S3, S4, and S5, the specific current increased with the increasing of scan rate. The anode and cathode peaks move towards higher and lower potentials with the increasing of scan rate, respectively. As can be seen from Fig. 7, the different morphologies of SrTiO<sub>3</sub> result in a slight shift in the position of reduction peak. For the SrTiO<sub>3</sub> rhombus particles (Fig. 7a), two redox peaks at 0.20 and 0.25 V can be observed. Sample S1 has a maximum integrated area in CV curve than that of other samples, indicating that the SrTiO<sub>3</sub> rhombus particles possess a highest electrochemical performance among all samples. With the increase of reaction time, the particles grow into the shape of a cube in orientation, but the integrated area in CV curve of Sample S2 is reduced as shown in Fig. 7b.

It is noteworthy that the homogeneous SrTiO<sub>3</sub> spherical nanoparticles (Fig. 7c) have a larger integrated area in CV curve than that of SrTiO<sub>3</sub> particles with cubes and spherical nanoparticles (Fig. 7d). In addition, the influence of impurities on the electrochemical properties of SrTiO<sub>3</sub> cannot be ignored. In Fig. 7e, the SrSO<sub>4</sub> impurity resulted in relatively large integrated area in CV curve of Sample S5. Derikvandi et al. [69] reported that the semiconductor photocatalyst has the best CV response which means the photocatalyst has a lower electron/hole (e<sup>-</sup>/h<sup>+</sup>) recombination and high photocatalytic activity for the photocatalytic degradation of organic dyes. Therefore, the best CV curve for Sample S1 implies that Sample S1 exhibits a highest photocatalytic activity.

The specific capacity of Samples S1, S2, S3, S4, and S5 were estimated through CV curve using Eq. (10). [5]

$$Q_s = \frac{1}{vm} \int_{v_i}^{v_f} I \times V dV, \quad (10)$$

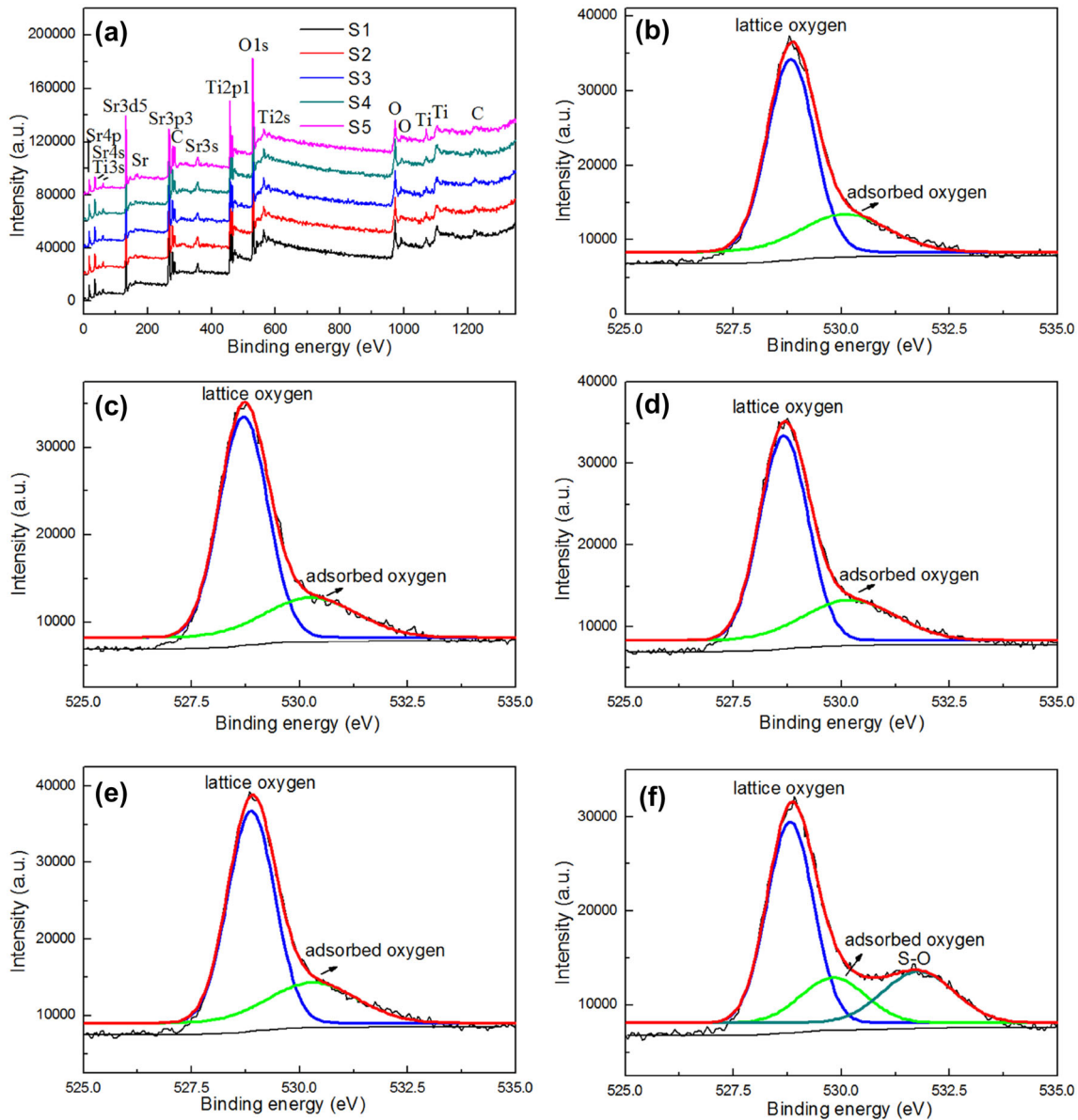


**Fig. 5** a XPS of survey spectra of Samples S1, S2, S3, S4, and S5. O1s high-resolution XPS spectra of Samples b S1, c S2, d S3, e S4, and f S5

**Table 3** XPS parameters of Samples S1, S2, S3, S4, and S5

Sample	Peak	$A_O/A_L$
S1	528.85    530.15    /	0.36
S2	528.71    530.19    /	0.35
S3	528.71    530.17    /	0.38
S4	528.92    530.11    /	0.37
S5	528.83    529.92    531.76	0.32

where,  $Q_s$ ,  $v$ ,  $m$ , and the integral term are the specific capacity ( $C \cdot g^{-1}$ ), scan rate ( $mV \cdot s^{-1}$ ), mass loading of active material (g), and anodic peak area in the CV

curve, respectively. Figure 6f shows the specific capacity vs. scan rate of Samples S1, S2, S3, S4, and S5. As scan rate increases,  $Q_s$  decreases due to the asynchronous movement of charges with respect to scan rate [5]. However, an abnormal phenomenon can be observed for the Sample S1 at the scan rates of 3 and 5  $mV \cdot s^{-1}$  due to the effect of high oxygen vacancy concentration. It clearly confirms that the Sample S4 shows the lowest electrochemical performance as compared to other  $SrTiO_3$  samples, which may be due to the heterogeneous particles, lower

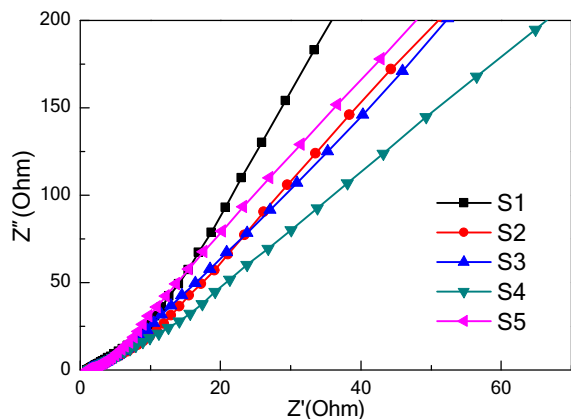


**Fig. 6** EIS spectra of Samples S1, S2, S3, S4, and S5

electrical conductivity, and lower facet-dependent, resulting in the reduced  $Q_s$  value.

### 3.6.3 Galvanostatic charge–discharge analysis

Figure 8a–e presents the typical charge–discharge curves of Samples S1, S2, S3, S4, and S5 at current density of 1, 1.2, 1.4, 1.6, 1.8, and 2 A/g. For all samples, the charge–discharge curves were non-linear which confirms the battery-type behavior of  $\text{SrTiO}_3$  particles. The variation tendencies for different samples are consistent with the CV measurements, suggesting that the as-prepared  $\text{SrTiO}_3$  particles have a pseudocapacitive behaviors. For the Sample S1, the longest discharge timing confirmed that the  $\text{SrTiO}_3$  rhombus particles can potentially increase the energy dissipation time. The  $\text{SrTiO}_3$  rhombus particles providing larger interfacial area are favorable for hydroxide ( $\text{OH}^-$ ) ions to participate in the reaction of faradaic type. The result indicates that Sample S1 has a highest photocatalytic activity as the photo-generated electron–hole pairs can react with  $\text{OH}^-$  to produce hydroxyl radical ( $\cdot\text{OH}$ ).  $\text{OH}$  attacks the organic dye to produce non-toxic and harmless products.

The specific capacitance of Samples S1, S2, S3, S4, and S5 can be calculated using Eq. (11) [5].

$$Q_{sc} (\text{F} \cdot \text{g}^{-1}) = \frac{I \cdot \Delta t}{\Delta V \cdot m}, \quad (11)$$

where  $Q_{sc}$ ,  $I$ ,  $\Delta t$ ,  $m$ , and  $\Delta V$  are the specific capacitance ( $\text{F} \cdot \text{g}^{-1}$ ), discharge current (A), discharge time (s), mass of active material (g) on the electrode, and working potential window (V), respectively. Figure 8f shows the specific capacitance vs. current

density of Samples S1, S2, S3, S4, and S5. It can be seen that Sample S1 exhibits high rate capacitance retention. After careful analysis, it is found that the  $\text{SrTiO}_3$  rhombus particles have three main merits: (1) the unique polyhedral structure enables intimate contact between particles; (2) high crystallinity enhances the electrical conductivity and makes it ease for charge transfer or transport across the special structure; (3) high electrochemical stability provides high charge storage for the  $\text{SrTiO}_3$  rhombus particles. This work confirms that crystal surface control is a key factor to consider in synthesizing and designing of perovskite-type photocatalyst to improve the electrochemical performance and photocatalytic activity.

## 3.7 Photocatalytic activity

### 3.7.1 Ultraviolet photocatalytic activity

Figure 9a shows the time-dependent photocatalytic degradation of congo red dye in the presence of Samples S1, S2, S3, S4, and S5 under ultraviolet light irradiation. The initial dye concentration and catalyst content are 1 mg/L and 1 g/L, respectively. According to literature [43], congo red dye is a stable and non-biodegradable molecule. The adsorption experiment shows that the adsorption percentage of congo red dye is about 8.5% for 0.5 h. The degradation percentage of each sample increases with the increasing of irradiation time. The degradation percentage of  $\text{SrTiO}_3$  samples under ultraviolet light irradiation for 150 min follows the order:  $\text{S1} > \text{S5} > \text{S4} > \text{S2} > \text{S3}$ .

The degradation curves of Samples S1, S2, S3, S4, and S5 are well fitted by a pseudo-first-order kinetics model. The pseudo-first-order kinetics rate ( $k$ ) for the photocatalytic degradation of congo red dye over the Samples S1, S2, S3, S4, and S5 can be obtained by the literature [43]. A plot of  $\ln(C_t/C_0)$  versus  $t$  for the Samples S1, S2, S3, S4, and S5 with different irradiation times for the congo red dye are shown in Fig. 9b. The  $k$  values of Samples S1, S2, S3, S4, and S5 can be obtained directly on the basis of Origin 8.0 software from the regression analysis of linear fitting curve in Fig. 9b. The rate constant  $k$  for Samples S1, S2, S3, S4, and S5 is obtained as 0.02788, 0.00661, 0.00429, 0.01207, and 0.01603  $\text{min}^{-1}$ , respectively. This implies that Sample S1 for the photocatalytic degradation of congo red dye under ultraviolet light irradiation has

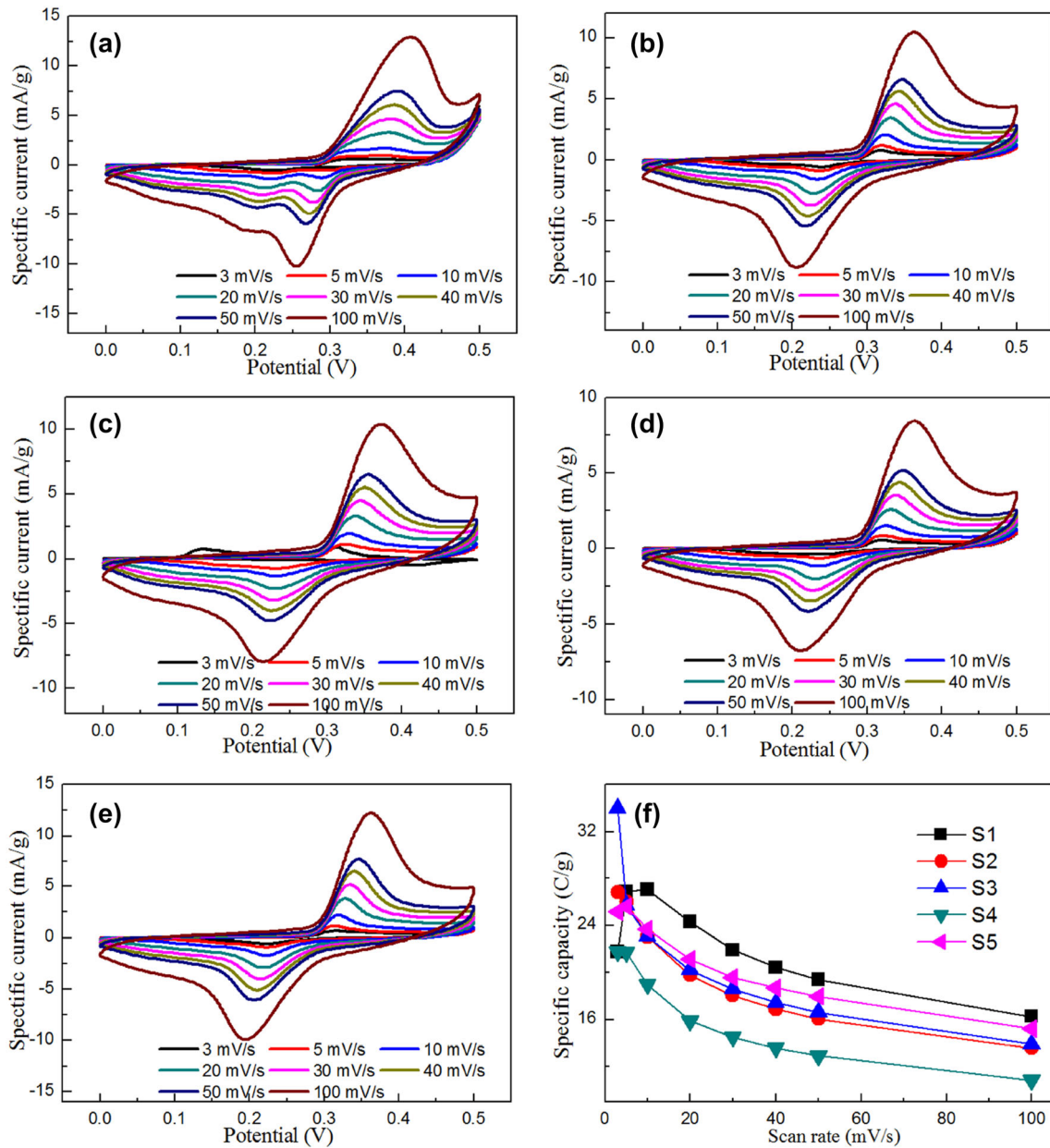


**Fig. 7** Cyclic voltammograms and specific capacity vs. scan rate of SrTiO<sub>3</sub>. **a** S1, **b** S2, **c** S3, **d** S4, **e** S5, and **f** specific capacity vs. scan rate of Samples S1, S2, S3, S4, and S5

a degradation percentage 6.50 times higher than that of Sample S3. The result confirms that Sample S1 exhibits a strongest photocatalytic activity for the photocatalytic degradation of congo red dye. The result further indicates that the crystal surface control plays a critical role in the aspect of improving photocatalytic activity. Sample S5 exhibits that a relatively high photocatalytic activity may be due to the effect of SrSO<sub>4</sub> impurity. The result indicates that the rate constant is directly proportional to photocatalytic activity of Samples S1, S2, S3, S4, and S5.

### 3.7.2 Visible photocatalytic activity

Figure 10a shows the time-dependent photocatalytic degradation of congo red dye in the presence of Samples S1, S2, S3, S4, and S5 under simulated sunlight irradiation for 180 min. The degradation percentage of SrTiO<sub>3</sub> samples follows the order: S1 > S2 > S4 > S3 > S5. The variation tendency is consistent with the optical absorption coefficient of visible light in UV–vis absorption spectrum. Figure 10b shows the first-order kinetic plots of Samples

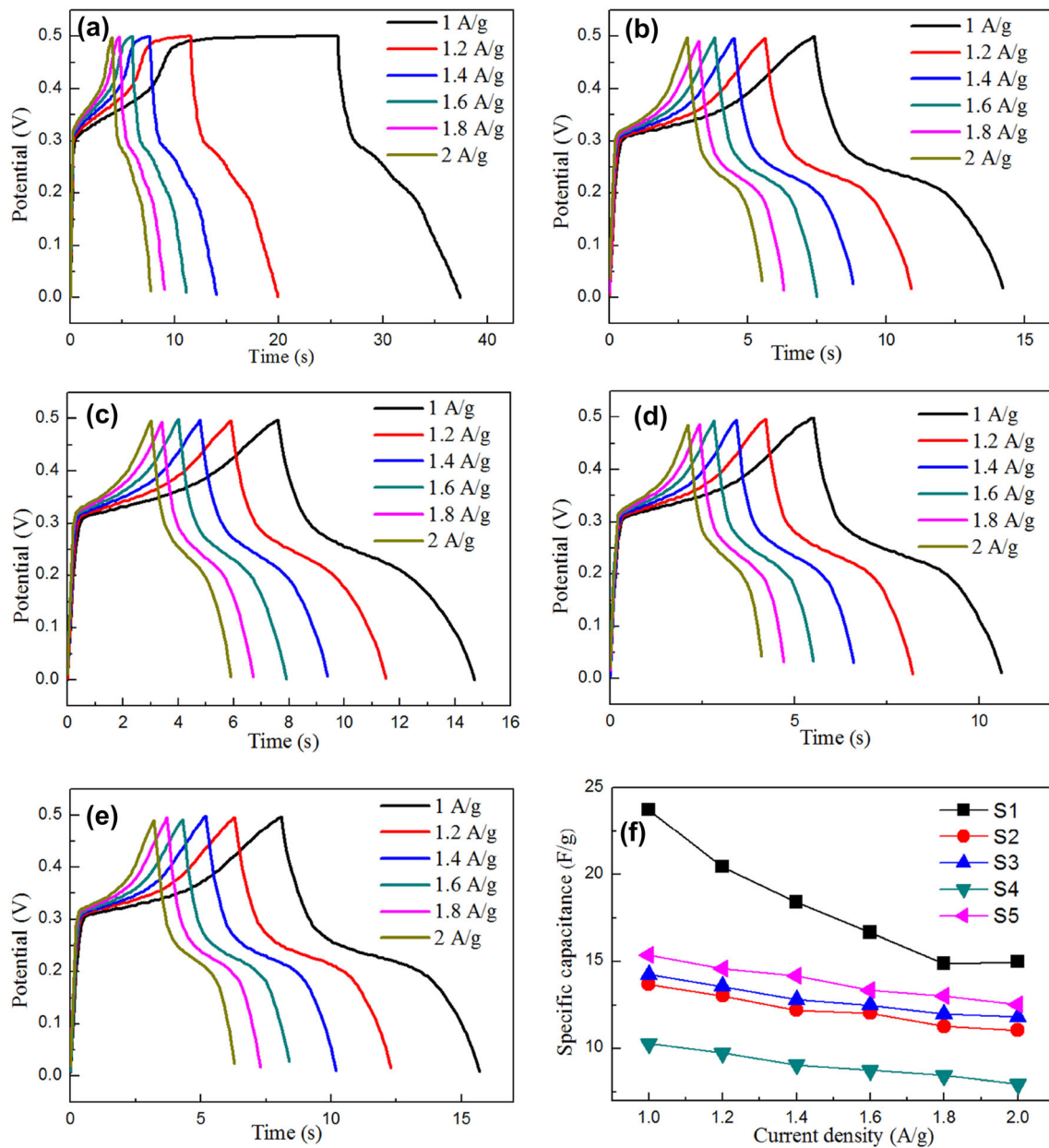


**Fig. 8** Charge–discharge curves and specific capacitances of SrTiO<sub>3</sub>. **a** S1, **b** S2, **c** S3, **d** S4, **e** S5, and **f** specific capacitance vs. current density of Samples S1, S2, S3, S4, and S5

S1, S2, S3, S4, and S5 for the photocatalytic degradation of congo red dye. The rate constant  $k$  for Samples S1, S2, S3, S4, and S5 is obtained as 0.01368, 0.00715, 0.00288, 0.00553, and 0.00210  $\text{min}^{-1}$ , respectively. The result indicates that Sample S1 has a highest visible photocatalytic activity, while Sample S5 exhibits a worst visible photocatalytic activity. Visible photocatalytic activity may be related to the synergistic effects of optical absorption coefficient,

oxygen vacancy concentration, impurity content, and charge utilization and separation efficiency for the SrTiO<sub>3</sub> particles.

### 3.8 Photocatalytic mechanism

Based on the above analysis, a possible photocatalytic mechanism and charge transfer process for the congo red dye degraded by pure SrTiO<sub>3</sub>, O (oxygen

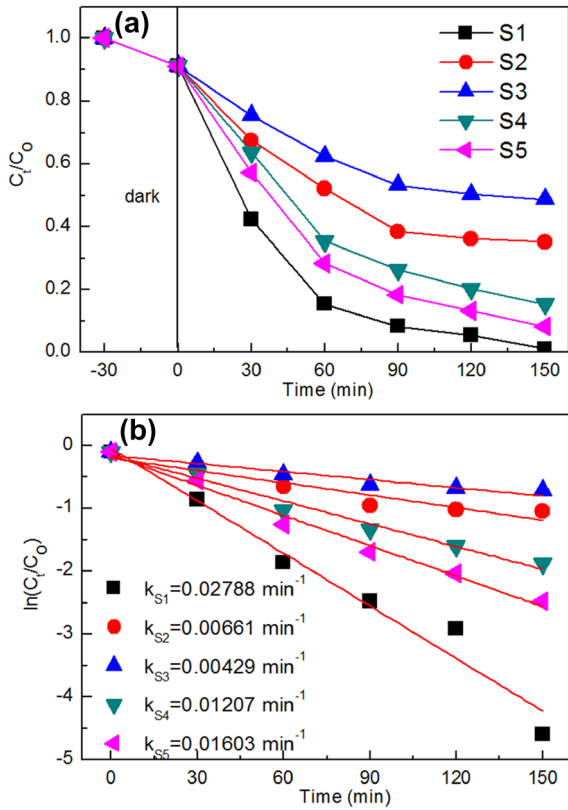
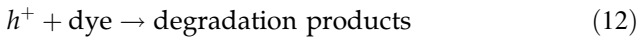


**Fig. 9** **a** Time-dependent photocatalytic degradation of congo red dye in the presence of Samples S1, S2, S3, S4, and S5 under ultraviolet light irradiation; **b** Plots of  $\ln(C_t/C_0)$  vs. irradiation time for Samples S1, S2, S3, S4, and S5

vacancy)— $\text{SrTiO}_3$ , or I (impurity) - $\text{SrTiO}_3$  was proposed as illustrated in Fig. 11. Silva et al. [70] reported that the  $\text{SrTiO}_3$  nanoparticles exhibit a photocatalytic activity mainly due to the valence band (VB) hole attack directly in the organic dye.



In the uniform  $\text{SrTiO}_3$  nanoparticles, the  $\cdot\text{OH}$  and  $\cdot\text{O}^{2-}$  are not formed due to the larger  $E_g$  value and no defect or impurity level, which is why the photocatalytic activity of Sample S3 is poor [71]. The dominant active species for the Sample S3 can be determined by the trapping experiment as shown in Fig. 12. The degradation percentage of Sample S3, Sample S3 + EDTA-2Na, Sample S3 + IPA, and Sample S3 + BQ is 46.5%, 32.3%, 85.6%, and 88.7%, respectively. The result confirmed that the hole ( $h^+$ ) plays an important role in the photo-degradation of congo red dye over Sample S3.

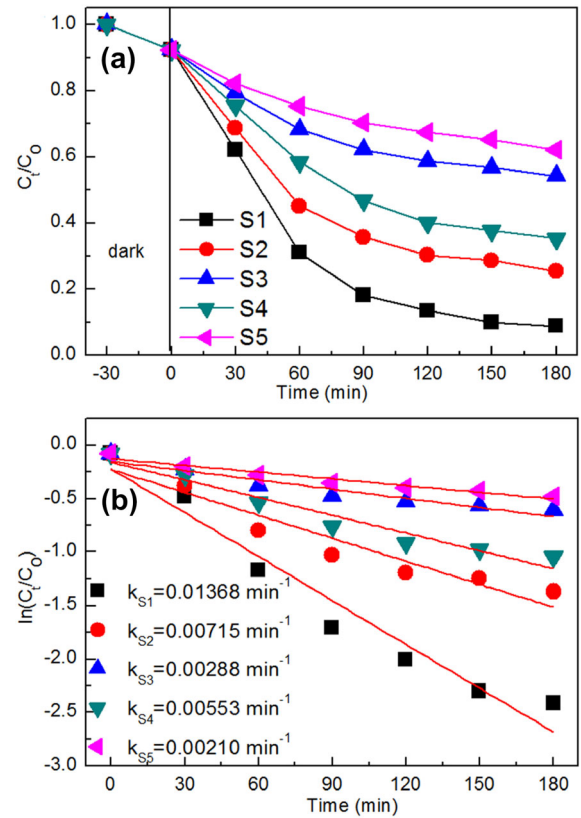


**Fig. 10** **a** Time-dependent photocatalytic degradation of congo red dye in the presence of Samples S1, S2, S3, S4, and S5 under simulated sunlight irradiation; **b** Plots of  $\ln(C_t/C_0)$  vs. irradiation time for Samples S1, S2, S3, S4, and S5

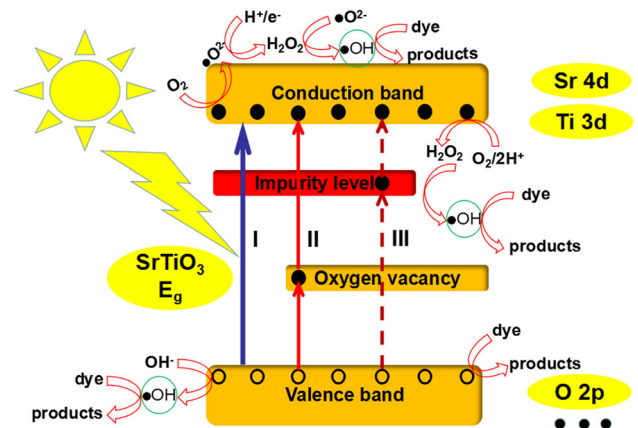
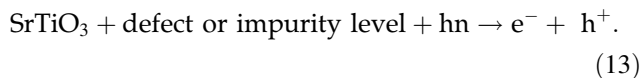


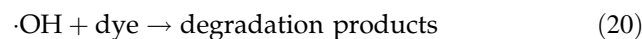
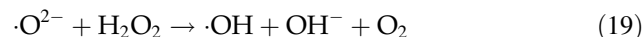
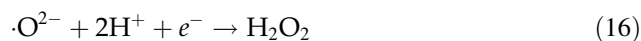
**Fig. 11** Photocatalytic mechanism for the congo red dye degraded by pure  $\text{SrTiO}_3$ , O (oxygen vacancy)— $\text{SrTiO}_3$ , and I (impurity)— $\text{SrTiO}_3$  under simulated sunlight irradiation

In the  $\text{SrTiO}_3$  photocatalytic system, Sr4d and Ti3d form the conduction band (CB) of  $\text{SrTiO}_3$ , and O2p, Sr4p, O2s, S4s, and Ti3p form the VB of  $\text{SrTiO}_3$  [72, 73]. Since the energy of incident simulated

sunlight is smaller than that of  $E_g$  value of  $\text{SrTiO}_3$  particles, it is difficult to excite the electron transition from VB to CB. However, the oxygen vacancy or impurity will provide a special energy level for  $\text{SrTiO}_3$  particles, which will promote the electron transition to CB. The charge carrier generation process can be recorded as follows:



The valence band holes or conduction band electrons can react with  $\text{OH}^-$  or  $\text{O}_2/\text{H}_2\text{O}_2$  to form  $\cdot\text{OH}$  as the redox potential of  $\text{OH}^-/\cdot\text{OH}$  is + 1.89 V versus NHE or the redox potential of  $\text{O}_2/\cdot\text{O}_2^-$  is - 0.33 V versus NHE [74–80]. Therefore, valence band holes easily react with hydroxide ions to form  $\cdot\text{OH}$ . The conduction band electrons react with oxygen to form  $\cdot\text{O}_2^-$ .  $\cdot\text{O}_2^-$  reacts with electrons and hydrogen ions again to produce hydrogen peroxide ( $\text{H}_2\text{O}_2$ ). In addition, electrons can react similarly with oxygen and hydrogen ions. Under the action of electrons or  $\cdot\text{O}_2^-$ , hydrogen peroxide will produce  $\cdot\text{OH}$ .  $\cdot\text{OH}$  reacts with dye molecule to produce non-toxic and harmless products. The simple chemical reaction can be expressed as follows:



The  $\text{SrTiO}_3$  rhombus particles have more crystal surface exposure, which is favorable for the photocatalytic degradation of organic dyes. To further confirm the role of  $h^+$ ,  $\cdot\text{OH}$ , and  $\cdot\text{O}_2^-$  in Sample S1 in the whole photocatalytic reaction process, Fig. 13 shows the trapping experiments of active species for the Sample S1 under simulated sunlight irradiation. The result shows that  $h^+$ ,  $\cdot\text{OH}$ , and  $\cdot\text{O}_2^-$  play critical roles in the photocatalytic reaction process. This indicates that the experimental results are consistent with the proposed photocatalytic mechanism. Therefore, the photocatalytic activity of  $\text{SrTiO}_3$  rhombus particles is obviously enhanced due to the synergistic effects of low recombination of electron–hole pair, high oxygen vacancy concentration, charge separation, and crystal surface exposure. In addition,  $\text{SrSO}_4$  impurity also plays an important role in suppressing the visible light photocatalytic activity of  $\text{SrTiO}_3$ .

## 4 Conclusion

Shape and phase-tunable  $\text{SrTiO}_3$  perovskite-type metal oxide with high oxygen vacancy concentration can be synthesized by different mineral acids including  $\text{HNO}_3$ ,  $\text{HCl}$ , or  $\text{H}_2\text{SO}_4$  and different

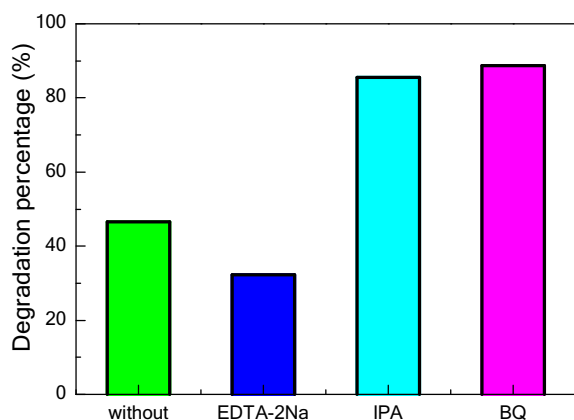


**Fig. 12** Trapping experiments of active species for Sample S3 under simulated sunlight irradiation

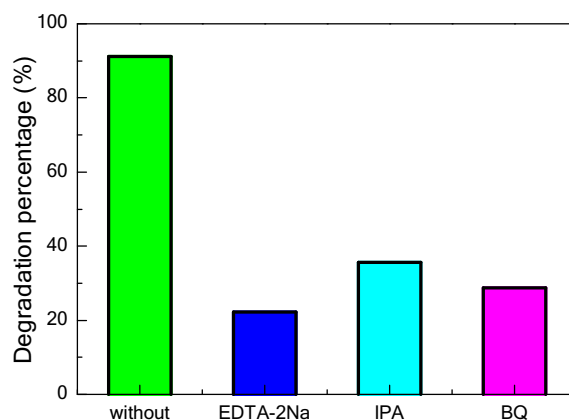


**Fig. 13** Trapping experiments of active species for Sample S1 under simulated sunlight irradiation

reaction times. The effects of phase purity, surface morphology, optical absorption coefficient, and charge transfer and separation efficiency on the optical, electrochemical performances and photocatalytic activity of SrTiO<sub>3</sub> perovskite-type metal oxide were systematically studied. The SrTiO<sub>3</sub> rhombus particles exhibit highest charge transfer and separation efficiency and photocatalytic activity for the photocatalytic degradation of congo red dye under simulated sunlight irradiation than that of the other SrTiO<sub>3</sub> samples. The high photocatalytic activity for the SrTiO<sub>3</sub> rhombus particles can be assigned to the synergistic effects of band edge position, oxygen vacancy concentration, impurity content, optical absorption coefficient, charge utilization and separation efficiency, and crystal surface exposure. The facet-dependent technology for improving the charge transfer and separation efficiency and photocatalytic activity can be used to synthesize other metal oxide semiconductors.

## Acknowledgements

This work was supported by Project 2019DB02 supported by NPL, CAEP, the Chongqing Natural Science Foundation (cstc2019jcyj-msxmX0310, cstc2018jcyjAX0599), the Talent Introduction Project (09924601), Major Cultivation Projects (18ZDPY01) and Research Project of Higher Education Teaching Reform (JGZC1903) of Chongqing Three Gorges University, the Science and Technology Research Program of Chongqing Education Commission of China (KJQN201901), and the Innovation Ability Improvement Project of Gansu Colleges and Universities (2019B-129).

## Compliance with ethical standards

**Conflict of interest** The authors declare that they have no conflict of interest.

## References

1. I. Arnay, J. Rubio-Zuazo, G.R. Castro, Impact of cleaning methods on the structural properties and morphology of SrTiO<sub>3</sub> surface. *Appl. Surf. Sci.* **427**, 561–565 (2018)
2. S. Yashodamma, G.P. Darshan, R.B. Basavaraj, H. Nagabhushana, Ultrasound assisted fabrication of SrTiO<sub>3</sub> nanopowders: Effect of electron beam induced structural and luminescence properties for solid state lightning and high temperature dosimetry applications. *Opt. Mater.* **92**, 386–398 (2019)
3. Y.X. Yan, H. Yang, Z. Yi, T. Xian, R.H. Li, X.X. Wang, Construction of Ag<sub>2</sub>S@CaTiO<sub>3</sub> heterojunction photocatalysts for enhanced photocatalytic degradation of dyes. *Desalin. Water Treat.* **170**, 349–360 (2019)
4. H.J. Gao, X.X. Zhao, H.M. Zhang, J.F. Chen, S.F. Wang, H. Yang, Construction of 2D/0D/2D face-to-face contact g-C<sub>3</sub>N<sub>4</sub>@Au@Bi<sub>4</sub>Ti<sub>3</sub>O<sub>12</sub> heterojunction photocatalysts for degradation of rhodamine B. *J. Electron Mater.* **49**, 5248–5259 (2020)
5. S. Shahabuddin, A. Numan, M.M. Shahid, R. Khanam, R. Saidur, A.K. Pandey, S. Ramesh, Polyaniline-SrTiO<sub>3</sub> nanocube based binary nanocomposite as highly stable electrode material for high performance supercapattery. *Ceram. Int.* **45**, 11428–11437 (2019)
6. U. Sandhya Shenoy, D. Krishna Bhat, Enhanced thermoelectric properties of vanadium doped SrTiO<sub>3</sub>: a resonant dopant approach. *J. Alloy. Compd.* **832**, 154958 (2020)
7. Y.M. Xia, Z.M. He, J.B. Su, S.Q. Zhu, B. Tang, Sustainable solar-light -driven SrTiO<sub>3</sub>/PbBiO<sub>2</sub>Br nanocomposites with enhanced photocatalytic activity. *J. Electron Mater.* **49**, 3259–3268 (2020)
8. S.T. Guan, R.S. Li, X.F. Sun, T. Xian, H. Yang, Construction of novel ternary Au/LaFeO<sub>3</sub>/Cu<sub>2</sub>O composite photocatalysts for RhB degradation via photo-Fenton catalysis. *Mater. Technol.* (2020). <https://doi.org/10.1080/10667857.2020.1782062>
9. B. Wang, S. Shen, L. Guo, Surface reconstruction of facet-functionalized SrTiO<sub>3</sub> nanocrystals for photocatalytic hydrogen evolution. *ChemCatChem* **8**, 798–804 (2016)
10. P.L. Hsieh, G. Naresh, Y.S. Huang, C.W. Tsao, Y.J. Hsu, L.J. Chen, M.H. Huang, Shape-tunable SrTiO<sub>3</sub> crystals revealing facet-dependent optical and photocatalytic properties. *J. Phys. Chem. C* **123**, 13664–13671 (2019)
11. H.J. Gao, C.X. Zheng, H. Yang, X.W. Niu, S.F. Wang, Construction of a CQDs/Ag<sub>3</sub>PO<sub>4</sub>/BiPO<sub>4</sub> heterostructure photocatalyst with enhanced photocatalytic degradation of rhodamine B under simulated solar irradiation. *Micromachines* **10**, 557 (2019)
12. S. Banakhojasteh, S. Beckert, R. Gläser, Modification of SrTiO<sub>3</sub> as a photocatalyst for hydrogen evolution from aqueous methanol solution. *J. Photochem. Photobiol. A* **366**, 48–54 (2018)
13. Y.X. Yan, H. Yang, Z. Yi, X.X. Wang, R.S. Li, T. Xian, Evolution of Bi nanowires from BiOBr nanoplates through a NaBH<sub>4</sub> reduction method with enhanced photodegradation performance. *Environ. Eng. Sci.* **37**, 64–77 (2020)



14. M. Ahmadi, M.S. Dorraji, M.H. Rasoulifard, A.R. Amani-Ghadim, The effective role of reduced-graphene oxide in visible light photocatalytic activity of wide band gap SrTiO<sub>3</sub> semiconductor. *Sep. Purif. Technol.* **228**, 115771 (2019)
15. M. Faisal, F.A. Harraz, A.A. Ismail, A.M. El-Toni, S.A. Al-Sayari, A. Al-Hajry, M.S. Al-Assiri, Polythiophene/mesoporous SrTiO<sub>3</sub> nanocomposites with enhanced photocatalytic activity under visible light. *Sep. Purif. Technol.* **190**, 33–44 (2018)
16. O. Dehghani Dastjerdi, H. Shokrollahi, H. Yang, The enhancement of the Ce-solubility limit and saturation magnetization in the Ce<sub>0.25</sub>Bi<sub>x</sub>Pr<sub>y</sub>Y<sub>2.75-x-y</sub>Fe<sub>5</sub>O<sub>12</sub> garnet synthesized by the conventional ceramic method. *Ceram. Int.* **46**, 2709–2723 (2020)
17. M. Klusáčková, R. Nebel, K.M. Macounová, M. Klementova, P. Krtil, Size control of the photo-electrochemical water splitting activity of SrTiO<sub>3</sub> nano-cubes. *Electrochim. Acta* **297**, 215–222 (2019)
18. L. Xu, Y. Zhao, W. Wang, H. Liu, R. Wang, Electrospinning fabrication of SrTiO<sub>3</sub> nanofibers and their photocatalytic activity. *Russ. J. Phys. Chem. A* **92**, 1237–1241 (2018)
19. T. Xian, H. Yang, J.F. Dai, Z.Q. Wei, J.Y. Ma, W.J. Feng, Photocatalytic properties of SrTiO<sub>3</sub> nanoparticles prepared by a polyacrylamide gel route. *Mater. Lett.* **65**, 3254–3257 (2011)
20. T. Puangpetch, T. Sreethawong, S. Yoshikawa, S. Chavadej, Synthesis and photocatalytic activity in methyl orange degradation of mesoporous-assembled SrTiO<sub>3</sub> nanocrystals prepared by sol–gel method with the aid of structure-directing surfactant. *J. Mol. Catal. A* **287**, 70–79 (2008)
21. S.T. Huang, W.W. Lee, J.L. Chang, W.S. Huang, S.Y. Chou, C.C. Chen, Hydrothermal synthesis of SrTiO<sub>3</sub> nanocubes: characterization, photocatalytic activities, and degradation pathway. *J. Taiwan Inst. Chem. E* **45**, 1927–1936 (2014)
22. H. Bantawal, U. Sandhya Shenoy, D. Krishna Bhat, Vanadium-doped SrTiO<sub>3</sub> nanocubes: insight into role of vanadium in improving the photocatalytic activity. *Appl. Surf. Sci.* **513**, 145858 (2020)
23. H. Bantawal, U. Sandhya Shenoy, D. Krishna, Bhat, Tuning the photocatalytic activity of SrTiO<sub>3</sub> by varying the Sr/Ti ratio: unusual effect of viscosity of the synthesis medium. *J. Phys. Chem. C* **122**, 20027–20033 (2018)
24. U. Sandhya Shenoy, H. Bantawal, D. Krishna, Bhat, Band engineering of SrTiO<sub>3</sub>: effect of synthetic technique and site occupancy of doped rhodium. *J. Phys. Chem. C* **122**, 27567–27574 (2018)
25. H. Bantawal, M. Sethi, U. Sandhya Shenoy, D. Krishna Bhat, Porous graphene wrapped SrTiO<sub>3</sub> nanocomposite: Sr–C bond as an effective coadjutant for high performance photocatalytic degradation of methylene blue. *ACS Appl. Nano Mater.* **2**, 6629–6636 (2019)
26. G. Canu, V. Buscaglia, Hydrothermal synthesis of strontium titanate: thermodynamic considerations, morphology control and crystallisation mechanisms. *CrystEngComm* **19**, 3867–3891 (2017)
27. M.N. Ha, F. Zhu, Z. Liu, L. Wang, L. Liu, G. Lu, Z. Zhao, Morphology-controlled synthesis of SrTiO<sub>3</sub>/TiO<sub>2</sub> heterostructures and their photocatalytic performance for water splitting. *RSC Adv.* **6**, 21111–21118 (2016)
28. S. Ouyang, P. Li, H. Xu, H. Tong, L. Liu, J. Ye, Bifunctional-nanotemplate assisted synthesis of nanoporous SrTiO<sub>3</sub> photocatalysts toward efficient degradation of organic pollutant. *ACS Appl. Mater. Int.* **6**, 22726–22732 (2014)
29. X. Zheng, K. Yan, Q. Kuang, J. Qiu, S. Yang, Mesoporous TiO<sub>2</sub> single crystals: facile shape-, size-, and phase-controlled growth and efficient photocatalytic performance. *ACS Appl. Mater. Int.* **5**, 3683–3690 (2013)
30. Z. Zheng, B. Huang, X. Qin, X. Zhang, Y. Dai, Facile synthesis of SrTiO<sub>3</sub> hollow microspheres built as assembly of nanocubes and their associated photocatalytic activity. *J. Colloid Interface Sci.* **358**, 68–72 (2011)
31. J. Li, H. Bai, W. Yi, J. Liu, Y. Li, Q. Zhang, G. Xi, Synthesis and facet-dependent photocatalytic activity of strontium titanate polyhedron nanocrystals. *Nano Res.* **9**, 1523–1531 (2016)
32. W. Zhou, G. Du, P. Hu, G. Li, D. Wang, H. Liu, H. Jiang, Nanoheterostructures on TiO<sub>2</sub> nanobelts achieved by acid hydrothermal method with enhanced photocatalytic and gas sensitive performance. *J. Mater. Chem.* **21**, 7937–7945 (2011)
33. W. Zhou, X. Liu, J. Cui, D. Liu, J. Li, H. Jiang, H. Liu, Control synthesis of rutile TiO<sub>2</sub> microspheres, nanoflowers, nanotrees and nanobelts via acid-hydrothermal method and their optical properties. *CrystEngComm* **13**, 4557–4563 (2011)
34. L. Shen, N. Bao, Y. Zheng, A. Gupta, T. An, K. Yanagisawa, Hydrothermal splitting of titanate fibers to single-crystalline TiO<sub>2</sub> nanostructures with controllable crystalline phase, morphology, microstructure, and photocatalytic activity. *J. Phys. Chem. C* **112**, 8809–8818 (2008)
35. T. Zhang, M. Liu, Y. Meng, B. Huang, X. Pu, X. Shao, A novel method for the synthesis of Ag<sub>3</sub>VO<sub>4</sub>/Ag<sub>2</sub>VO<sub>2</sub>PO<sub>4</sub> heterojunction photocatalysts with improved visible-light photocatalytic properties. *Sep. Purif. Technol.* **206**, 149–157 (2018)
36. P. Scherrer, Bestimmung der Grösse und der inneren struktur von kolloidteilchen mittels röntgenstrahlen. *Nachr. Ges. Wiss. Göttingen* **26**, 98 (1918)

37. J.I. Langford, A.J.C. Wilson, Scherrer after sixty years: a survey and some new results in the determination of crystallite size. *J. Appl. Cryst.* **11**, 102 (1978)
38. V. Uvarov, I. Popov, Metrological characterization of X-ray diffraction methods for determination of crystallite size in nano-scale materials. *Mater. Charact.* **85**, 111 (2013)
39. S. Piskunov, E. Heifets, R.I. Eglitis, G. Borstel, Bulk properties and electronic structure of SrTiO<sub>3</sub>, BaTiO<sub>3</sub>, PbTiO<sub>3</sub> perovskites: an ab initio HF/DFT study. *Comput. Mater. Sci.* **29**, 165–178 (2004)
40. S.F. Wang, Q. Li, X.T. Zu, X. Xiang, W. Liu, S. Li, Phase controlled synthesis of (Mg, Ca, Ba)-ferrite magnetic nanoparticles with high uniformity. *J. Magn. Magn. Mater.* **419**, 464–475 (2016)
41. F. Dang, K.I. Mimura, K. Kato, H. Imai, S. Wada, H. Haneda, M. Kuwabara, Growth of monodispersed SrTiO<sub>3</sub> nanocubes by thermohydrolysis method. *CrystEngComm* **13**, 3878–3883 (2011)
42. R.L. Penn, J.F. Banfield, Oriented attachment and growth, twinning, polytypism, and formation of metastable phases: Insights from nanocrystalline TiO<sub>2</sub>. *Am. Miner.* **83**, 1077–1082 (1998)
43. H. Gao, H. Yang, S. Wang, Hydrothermal synthesis, growth mechanism, optical properties and photocatalytic activity of cubic SrTiO<sub>3</sub> particles for the degradation of cationic and anionic dyes. *Optik* **175**, 237–249 (2018)
44. M. Gopal, W.M. Chan, L.C. De Jonghe, Room temperature synthesis of crystalline metal oxides. *J. Mater. Sci.* **32**, 6001–6008 (1997)
45. B. Tian, F. Chen, J. Zhang, M. Anpo, Influences of acids and salts on the crystalline phase and morphology of TiO<sub>2</sub> prepared under ultrasound irradiation. *J. Colloid Interface Sci.* **303**, 142–148 (2006)
46. Z. Yi, Y. Zeng, H. Wu, X. Chen, Y. Fan, H. Yang, Y. Tang, Y. Yi, J. Wang, P. Wu, Synthesis, surface properties, crystal structure and dye-sensitized solar cell performance of TiO<sub>2</sub> nanotube arrays anodized under different parameters. *Results Phys.* **15**, 102609 (2019)
47. M.R. McLellan, L.R. Lind, R.W. Kime, Hue angle determinations and statistical analysis for multiquadrant hunter L, a, b data. *J. Food Qual.* **18**, 235–240 (1995)
48. H. Gao, H. Yang, S. Wang, Comparative study on optical and electrochemical properties of MFe<sub>2</sub>O<sub>4</sub> (M = Mg, Ca, Ba) nanoparticles. *T. Indian Ceram. Soc.* **77**, 150–160 (2018)
49. P. Yu, H. Yang, X. Chen, Z. Yi, W. Yao, J. Chen, Y. Yi, P. Wu, Ultra-wideband solar absorber based on refractory titanium metal. *Renew. Energy* **158**, 227–235 (2020)
50. H. Shen, Y. Lu, Y. Wang, Z. Pan, G. Cao, X. Yan, G.L. Fang, Effects of different backbone binders on the characteristics of zirconia parts using wax-based binder system via ceramic injection molding. *J. Adv. Ceram.* **5**, 321–328 (2016)
51. J. Tauc, A. Menth, States in the gap. *J. Non-Cryst. Solids* **8**, 569–585 (1972)
52. D. Li, J. Gao, P. Cheng, J. He, Y. Yin, Y. Hu, L. Chen, Y. Cheng, J. Zhao, 2D boron sheets: structure, growth, and electronic and thermal transport properties. *Adv. Funct. Mater.* **30**, 1904349 (2020)
53. H. Wu, H. Jile, Z. Chen, D. Xu, Z. Yi, X. Chen, J. Chen, W. Yao, P. Wu et al., Fabrication of ZnO@MoS<sub>2</sub> nanocomposite heterojunction arrays and their photoelectric properties. *Micromachines* **11**, 189 (2020)
54. S. Wang, C. Chen, Y. Li, Q. Zhang, Y. Li, H. Gao, Synergistic effects of optical and photoluminescence properties, charge transfer, and photocatalytic activity in MgAl<sub>2</sub>O<sub>4</sub>:Ce and Mn-codoped MgAl<sub>2</sub>O<sub>4</sub>:Ce phosphors. *J. Electron. Mater.* **48**, 6675–6685 (2019)
55. M. Golkari, H. Shokrollahi, H. Yang, The influence of Eu cations on improving the magnetic properties and promoting the Ce solubility in the Eu, Ce-substituted garnet synthesized by the solid state route. *Ceram. Int.* **46**, 8553–8560 (2020)
56. H. Huan, H. Jile, Y. Tang, X. Li, Z. Yi, X. Gao, X. Chen, J. Chen, P. Wu, Fabrication of ZnO@Ag@Ag<sub>3</sub>PO<sub>4</sub> ternary heterojunction: superhydrophilic properties, antireflection and photocatalytic properties. *Micromachines* **11**, 309 (2020)
57. F. Zhao, X. Chen, Z. Yi, F. Qin, Y. Tang, W. Yao, Z. Zhou, Y. Yi, Study on the solar energy absorption of hybrid solar cells with trapezoid-pyramidal structure based PEDOT:PSS/c-Ge. *Solar Energy* **204**, 635–643 (2020)
58. S.F. Wang, H. Gao, G. Sun, Y. Li, Y. Wang, H. Liu, C. Chen, L. Yang, Structure characterization, optical and photoluminescence properties of scheelite-type CaWO<sub>4</sub> nanophosphors: effects of calcination temperature and carbon skeleton. *Opt. Mater.* **99**, 109562 (2020)
59. D.E. Haycock, C.J. Nicholls, D.S. Urch, M.J. Webber, G. Wiech, The electronic structure of magnesium dialuminium tetraoxide (spinel) using X-ray emission and X-ray photoelectron spectroscopies. *J. Chem. Soc. Dalton* **12**, 1785–1790 (1978)
60. F. Li, L. Zhang, X. Chen, Y.L. Liu, S.G. Xu, S.K. Cao, Synergistically enhanced photocatalytic reduction of CO<sub>2</sub> on N-Fe codoped BiVO<sub>4</sub> under visible light irradiation. *Phys. Chem. Chem. Phys.* **19**, 21862–21868 (2017)
61. D. Zhang, H. Liu, C. Su, H. Li, Y. Geng, Combustion synthesis of highly efficient Bi/BiOBr visible light photocatalyst with synergetic effects of oxygen vacancies and surface plasma resonance. *Sep. Purif. Technol.* **218**, 1–7 (2019)
62. S. Contarini, J.W. Rabalais, Ion bombardment-induced decomposition of Li and Ba sulfates and carbonates studied

- by X-ray photoelectron spectroscopy. *J. Electron Spectrosc.* **35**, 191–201 (1985)
63. X.X. Wang, Y. Li, M.C. Liu, L.B. Kong, Fabrication and electrochemical investigation of  $MWO_4$  ( $M = Co, Ni$ ) nanoparticles as high-performance anode materials for lithium-ion batteries. *Ionics* **24**, 363–372 (2018)
64. J. Lin, R. Zong, M. Zhou, Y. Zhu, Photoelectric catalytic degradation of methylene blue by  $C_{60}$ -modified  $TiO_2$  nanotube array. *Appl. Catal. B* **89**, 425–431 (2009)
65. S. Zhu, T. Xu, H. Fu, J. Zhao, Y. Zhu, Synergetic effect of  $Bi_2WO_6$  photocatalyst with  $C_{60}$  and enhanced photoactivity under visible irradiation. *Environ. Sci. Technol.* **41**, 6234–6239 (2007)
66. S. Wang, H. Gao, Y. Wei, Y. Li, X. Yang, L. Fang, L. Lei, Insight into the optical, color, photoluminescence properties, and photocatalytic activity of the N–O and C–O functional groups decorating spinel type magnesium aluminate. *CrytEngComm* **21**, 263–277 (2019)
67. Y. Tang, X. Zhang, Y. Ma, X. Wang, C. Su, D. Zhang, Y. Geng, One-dimensional core-shell  $Zn_{0.1}Cd_{0.9}S/SnIn_4S_8$  heterojunction for enhanced visible light photocatalytic degradation. *Sep. Purif. Technol.* **230**, 115896 (2020)
68. S. Liang, T. Zhang, D. Zhang, X. Pu, X. Shao, W. Li, J. Dou, One-pot combustion synthesis and efficient broad spectrum photoactivity of  $Bi/BiOBr:Yb, Er/C$  photocatalyst. *J. Am. Ceram. Soc.* **101**, 3424–3436 (2018)
69. H. Derikvandi, A. Nezamzadeh-Ejhi, A comprehensive study on electrochemical and photocatalytic activity of  $SnO_2$ - $ZnO$ /clinoptilolite nanoparticles. *J. Mol. Catal. A* **426**, 158–169 (2017)
70. L.F. da Silva, O.F. Lopes, V.R. de Mendonça, K.T. Carvalho, E. Longo, C. Ribeiro, V.R. Mastelaro, An understanding of the photocatalytic properties and pollutant degradation mechanism of  $SrTiO_3$  nanoparticles. *Photochem. photobiol.* **92**, 371–378 (2016)
71. Y. Luo, B. Deng, Y. Pu, A. Liu, J. Wang, K. Ma, L. Dong, Interfacial coupling effects in  $g-C_3N_4/SrTiO_3$  nanocomposites with enhanced  $H_2$  evolution under visible light irradiation. *Appl. Catal. B* **247**, 1–9 (2019)
72. K. Van Benthem, R.H. French, W. Sigle, C. Elsässer, M. Rühle, Valence electron energy loss study of Fe-doped  $SrTiO_3$  and a  $\Sigma 13$  boundary: electronic structure and dispersion forces. *Ultramicroscopy* **86**, 303–318 (2001)
73. V. Mishra, A. Sati, M.K. Warshi, A.B. Phatangare, S. Dhole, V.N. Bhoraskar, P.R. Sagdeo, Effect of electron irradiation on the optical properties of  $SrTiO_3$ : an experimental and theoretical investigations. *Mater. Res. Exp.* **5**, 036210 (2018)
74. Y. Zhang, P. Wu, Z. Zhou, X. Chen, Z. Yi, J. Zhu, T. Zhang, H. Jile, Study on temperature adjustable terahertz metamaterial absorber based on vanadium dioxide. *IEEE Access* **8**, 85154–85161 (2020)
75. Y. Xia, Z. He, J. Su, K. Hu, Construction of novel  $Cu_2O/PbBiO_2Br$  composites with enhanced, photocatalytic activity. *J. Mater. Sci. Mater. Electron.* **30**, 9843–9854 (2019)
76. C. Cai, S. Han, W. Liu, K. Sun, L. Qiao, S. Li, X. Zu, Tuning catalytic performance by controlling reconstruction process in operando condition. *Appl. Catal. B* **260**, 118103 (2020)
77. F. Qin, X. Chen, Z. Yi, W. Yao, H. Yang, Y. Tang, Y. Yi, H. Li, Y. Yi, Ultra-broadband and wide-angle perfect solar absorber based on  $TiN$  nanodisk and  $Ti$  thin film structure. *Solar Energy Mater. Sol. C* **211**, 110535 (2020)
78. Z. He, Y. Xia, J. Su, B. Tang, Fabrication of magnetically separable  $NiFe_2O_4/Bi_{24}O_{31}Br_{10}$  nanocomposites and excellent photocatalytic performance under visible light irradiation. *Opt. Mater.* **88**, 195–203 (2019)
79. Y. Yan, H. Yang, Z. Yi, R. Li, T. Xian, Design of ternary  $CaTiO_3/g-C_3N_4/AgBr$  Z-scheme heterostructured photocatalysts and their application for dye photodegradation. *Solid State Sci.* **100**, 106102 (2020)
80. Y. Xia, Z. He, J. Su, X. Li, B. Tang, One-step construction of novel  $PbBiO_2Br/ZnO$  heterojunction composites with enhanced photocatalytic activity. *Phys. Status Solidi A* **216**, 1900406 (2019)

**Publisher's Note** Springer Nature remains neutral with regard to jurisdictional claims in published maps and institutional affiliations.